RSC Advances

PAPER

Published on 11 August 2026

Cite this: DOI: 10.1039/d6ra05041g

Superexchange disruption and anomalous magnetic anisotropy in $Fe_{3-x}Lu_xO_4$ nanoparticles

N. T. Dang,[ab] D. P. Kozlenko,[c] S. E. Kichanov,[c] A. V. Rutkauskas,*[c] N. H. Nam,[d] N. D. Minh,[d] D. P. T. Tien,*[e] N. T. Nguyen,[cef] T. A. Tran,[g] Y. D. Mitskevich,[h] A. A. Kharchanka,[h] J. A. Fedotova,[h] G. S. Rymski,[i] A. L. Zhaludkevich,[i] Pham Thanh Phong *[jk] and Truong-Tho Nguyen *[f]

Magnetite Fe_3O_4 nanoparticles are widely regarded as a prototypical ferrimagnetic spinel system; however, their magnetic response at the nanoscale increasingly reflects a non-ideal regime where exchange interactions, structural disorder, and surface-driven effects coexist in a strongly coupled manner. In this work, we investigate $Fe_{3-x}Lu_xO_4$ ($0 \leq x \leq 0.3$) nanoparticles to elucidate how non-magnetic rare-earth substitution modifies this coupled magnetostructural landscape. Using a combination of X-ray and neutron powder diffraction, ^{57}Fe Mössbauer spectroscopy, and magnetization measurements, we show that Lu^{3+} incorporation does not act as a simple magnetic diluent, but instead induces a restructuring of cation distribution, lattice strain, and local exchange topology. Lu^{3+} ions preferentially occupy octahedral B sites, leading to progressive disruption of J_{AB} superexchange connectivity and the emergence of locally decoupled A-site Fe^{3+} clusters. This disruption is accompanied by increased structural coherence length and enhanced magnetic inhomogeneity, reflected in the coexistence of blocked, superparamagnetic, and defect-associated spin populations. The magnetic response arises from the competition between exchange dilution, surface spin disorder, and strain-mediated anisotropy. Magnetometry reveals simultaneous suppression of saturation magnetization and enhancement of coercivity with increasing Lu content, indicating that magnetization reversal becomes increasingly governed by anisotropy barriers and pinning effects rather than coherent ferrimagnetic alignment. The effective anisotropy constant $K_1(T)$ exhibits strong deviations from Callen–Callen scaling, with anomalously low exponents ($q = 1.26$–1.83), highlighting the breakdown of bulk-like spin–orbit scaling under finite-size and surface-dominated conditions. Although $K_1(T)$ follows a Bloch-type behavior, consistent with spin-wave excitations, it is strongly renormalized by nanoscale disorder. These findings demonstrate that Lu substitution drives Fe_3O_4 nanoparticles into a non-ideal magnetic regime where ferrimagnetic order, surface spin frustration, and structural heterogeneity are inseparably intertwined through cation redistribution, exchange-path fragmentation, and surface-mediated anisotropy fluctuations.

Received 9th June 2026
Accepted 6th August 2026

DOI: 10.1039/d6ra05041g

rsc.li/rsc-advances

I. Introduction

Fe_3O_4 nanoparticles have emerged as one of the most intensively investigated magnetic nanomaterials because their collective magnetic response can be precisely tuned through structural confinement, cation distribution, and surface engineering. Their ability to exhibit superparamagnetic (SPM) behavior together with efficient magnetic energy dissipation

[a]Institute of Research and Development, Duy Tan University, 550000 Danang, Vietnam
[b]Faculty of Environmental and Natural Sciences, Duy Tan University, 550000 Danang, Vietnam
[c]Frank Laboratory of Neutron Physics, Joint Institute for Nuclear Research, 141980 Dubna, Russia. E-mail: ranton@nf.jinr.ru
[d]Faculty of Physics, VNU University of Science, Vietnam National University, Hanoi, 334 Nguyen Trai, Thanh Xuan, Hanoi, Vietnam
[e]Institute of Oceanography, Vietnam Academy of Science and Technology, 650000 Nha Trang, Vietnam. E-mail: doantien@io.vast.vn
[f]Faculty of Electronics, Electrical Engineering and Material Technology, University of Sciences, Hue University, 530000 Hue, Vietnam. E-mail: truongtho@hueuni.edu.vn
[g]Department of Engineering Physics, Ho Chi Minh City University of Technology and Engineering, Ho Chi Minh City, Vietnam
[h]Research Institute for Nuclear Problems of Belarusian State University, St. Bobruiskaya 11, 220006 Minsk, Belarus
[i]Scientific-Practical Materials Research Center of the National Academy of Sciences of Belarus, 220072 Minsk, Belarus
[j]Laboratory of Magnetism and Magnetic Materials, Science and Technology Advanced Institute, Van Lang University, Ho Chi Minh City, Vietnam. E-mail: phamthanhphong@vlu.edu.vn
[k]Faculty of Applied Technology, Van Lang School of Technology, Van Lang University, Ho Chi Minh City, Vietnam

under alternating magnetic fields has made them highly attractive for spintronic technologies and biomedical applications, including magnetic hyperthermia, magnetic resonance imaging, targeted drug delivery, and nanotheranostics.[1–8] However, the growing technological reliance on Fe_3O_4-based nanostructures has also exposed a fundamental scientific challenge: magnetic behavior at the nanoscale often deviates substantially from the predictions of conventional bulk ferrimagnetic models.

Crystallographically, Fe_3O_4 adopts an inverse spinel structure (AB_2O_4), where Fe^{3+} ions occupy the tetrahedral A sites, while the octahedral B sites contain mixed Fe^{2+}/Fe^{3+} valence states. In bulk magnetite, magnetic ordering is primarily governed by the strong antiferromagnetic inter-sublattice exchange interaction J_{AB}, which aligns the magnetic moments of the A and B sublattices antiparallel and stabilizes long-range ferrimagnetic ordering with a high Curie temperature ($T_C \approx 840$ K) and large saturation magnetization ($M_s \approx 98$ emu g^{-1}).[9,10] Nevertheless, this classical ferrimagnetic framework implicitly assumes relatively stable exchange pathways and well-ordered cation distributions. Such assumptions become increasingly questionable in nanostructured systems, where finite-size effects, surface spin disorder, broken exchange symmetry, and local structural heterogeneity can generate competing magnetic interactions that are absent or negligible in bulk materials.

When the particle size of Fe_3O_4 is reduced to the nanoscale regime, its magnetic behavior undergoes profound transformations that cannot be fully explained using conventional bulk ferrimagnetic models. Below the critical multidomain-to-single-domain threshold (~80–90 nm), magnetic reversal becomes increasingly governed by anisotropy-driven coherent spin dynamics rather than domain-wall motion.[8,10] Upon further reduction to approximately 25–30 nm, thermal fluctuations become comparable to the magnetic anisotropy energy barrier, resulting in the emergence of superparamagnetic behavior at room temperature.[8,10] However, this size-driven transition is accompanied by increasingly complex magnetic disorder effects arising from finite-size confinement and surface-dominated interactions.

At nanoscale dimensions, the large surface-to-volume ratio disrupts the balance of magnetic exchange interactions through broken superexchange pathways, reduced spin coordination, and local symmetry distortion. Consequently, surface spin canting, non-collinear spin configurations, and frustrated magnetic states may emerge, often leading to substantial suppression of saturation magnetization and deviations from ideal ferrimagnetic ordering.[8,11–13] Importantly, growing experimental evidence suggests that these magnetic anomalies cannot be attributed solely to surface effects, but instead arise from a cooperative interplay between crystallite size, particle morphology, cation redistribution, structural heterogeneity, and competing exchange interactions.[4,7,8,11,13]

In this context, chemical substitution has evolved from a simple tuning strategy into a powerful route for engineering the magnetic energy landscape of ferrite nanoparticles.[7,8,10,13] Among various dopants, rare-earth (RE) ions are particularly intriguing because their localized 4f electrons introduce strong spin–orbit coupling and enhanced magnetocrystalline anisotropy, while their relatively large ionic radii can induce substantial lattice distortion and exchange imbalance. As a result, RE incorporation may not merely perturb the ferrimagnetic matrix but fundamentally reorganize exchange pathways, thereby promoting emergent magnetic states beyond the predictions of classical ferrimagnetic theory.

Although RE substitution is widely employed to tune the magnetic properties of Fe_3O_4 nanoparticles, the resulting evolution of saturation magnetization (M_s) remains highly inconsistent across the literature. In many systems, low RE concentrations (<1–2 at%) lead to enhanced magnetization, whereas higher doping levels typically suppress M_s.[7,8,13] For example, Kowalik *et al.*[14] reported that Y^{3+} incorporation initially increases M_s from 65 to 75 emu g^{-1} at $x = 0.01$ in $Fe_{3-x}Y_xO_4$ nanoparticles, followed by a progressive reduction at higher concentrations. Similarly, Hazarika *et al.*[15] observed a non-monotonic magnetic response in $Fe_{3-x}Tb_xO_4$ nanoparticles, where M_s decreases from 70.6 to 51.7 emu g^{-1} for $x =$ 0–0.05 before sharply increasing to 96.1 emu g^{-1} at $x = 0.07$. Furthermore, Rękorajska *et al.* observed a gradual reduction in M_s at higher Tb doping concentrations.[16] Interestingly, opposite trends have been reported for Dy-doped systems depending on nanoparticle morphology and structural organization.[17,18] In $Fe_{3-x}Dy_xO_4$ flower-like nanoclusters, Dy^{3+} substitution markedly enhances M_s from 55.3 emu g^{-1} to 85.8 emu g^{-1} over the range $x = 0.082$–0.209.[17] In contrast, Park *et al.*[18] found that M_s in $Fe_{3-x}Dy_xO_4$ dispersed nanoparticles gradually decreases from 59.2 to 8.5 emu g^{-1} as x increases from 0 to 0.8, before partially recovering to 50.5 emu g^{-1} at $x = 1.6$.

More importantly, these contradictory magnetic responses cannot be fully reconciled within the conventional interpretation based solely on simple cation substitution or site occupancy arguments. Existing models generally assume that RE^{3+} incorporation modifies the ferrimagnetic balance through preferential occupation of octahedral sites and associated Fe^{2+}/Fe^{3+} redistribution.[8,15] However, the strong dependence of M_s on particle morphology, structural heterogeneity, and doping concentration suggests that RE incorporation simultaneously perturbs multiple coupled parameters, including exchange pathways, local lattice symmetry, magnetic anisotropy, and spin coherence. Consequently, the magnetic evolution of RE-doped Fe_3O_4 nanoparticles appears to be governed not by a single-factor mechanism, but by a complex competition between ferrimagnetic ordering, spin canting, exchange frustration, and disorder-driven magnetic fluctuations. This unresolved complexity represents a critical limitation for the predictive design of ferrite nanomaterials. Despite extensive experimental efforts, a unified mechanistic framework capable of explaining the highly non-linear and often contradictory magnetic behavior of RE-substituted Fe_3O_4 nanoparticles remains lacking.

Motivated by the unresolved and often contradictory magnetic responses observed in RE-doped Fe_3O_4 nanoparticles, we investigate Lu substitution as a mechanistic probe to disentangle the competing roles of cation redistribution, lattice distortion, and exchange interaction perturbation. Unlike

magnetic rare-earth ions, Lu^{3+} possesses a fully filled $4f^{14}$ electronic configuration and is effectively non-magnetic, thereby eliminating direct 4f–3d magnetic coupling effects. This unique characteristic enables the isolation of purely structural and electronic perturbations induced by RE incorporation, without introducing additional magnetic complexity from the dopant itself.

By systematically varying Lu concentration in Fe_3O_4 nanoparticles synthesized *via* chemical coprecipitation, we combine X-ray and neutron powder diffraction, Mössbauer spectroscopy, and magnetization measurements to correlate structural evolution with magnetic response. This approach allows us to critically evaluate whether the observed magnetic anomalies arise primarily from cation redistribution within the inverse spinel lattice or from deeper modifications of exchange pathways and local spin configurations induced by lattice distortion.

II. Experimental details

Lutetium-doped magnetite nanoparticles $Fe_{3-x}Lu_xO_4$ ($x = 0$, 0.075, 0.15, 0.225, and 0.3) were synthesized by the chemical coprecipitation method. $FeCl_3 \cdot 6H_2O$, $FeSO_4 \cdot 7H_2O$, and $Lu(NO_3)_3 \cdot 4H_2O$ were used as precursor materials and mixed in a molar ratio of $(2 - x) : 1 : x$, corresponding to the nominal composition $Fe_{3-x}Lu_xO_4$. The synthesis was carried out under a flowing N_2 atmosphere to suppress oxidation of Fe^{2+} ions and prevent the formation of α-FeOOH impurities. A 25% NH_4OH solution was used as the precipitating agent. After precipitation, the obtained precipitates were washed with distilled water and vacuum-dried at 80 °C.

The morphological properties of the synthesized samples were examined by scanning electron microscopy (SEM) and transmission electron microscopy (TEM). SEM images were acquired without gold coating using a JEOL JSM-IT200 scanning electron microscope operated at an accelerating voltage of 15.0 kV and a magnification of 10 000×. Energy-dispersive X-ray spectroscopy (EDX) was performed in conjunction with SEM to analyze the elemental composition. TEM images were acquired using a Thermo Scientific Talos F200i microscope operated at an accelerating voltage of 200 kV. The phase composition, crystal structure, and magnetic structure were examined by a combination of room-temperature X-ray diffraction (XRD) and neutron powder diffraction (NPD). XRD patterns were recorded on a D8 Advance Eco diffractometer (Bruker) employing a Cu-Kα source ($\lambda_1 = 1.5406$ Å, $\lambda_2 = 1.5444$ Å, with an intensity ratio $I_2/I_1 = 0.48$). The NPD measurements were carried out on the DN-6 time-of-flight diffractometer at the IBR-2 pulsed reactor (JINR, Russia).[19] Analysis of the diffraction data was performed through Rietveld refinement using the FullProf package.[20]

^{57}Fe Mössbauer spectra were collected in transmission geometry using a SEE Co. (USA) spectrometer equipped with a 20 mCi ^{57}Co/Rh radioactive source (Ritverc, Russia). Measurements were performed at 20 and 300 K employing a CCS-850 closed-cycle cryogenic system (Janis, USA). The velocity scale was calibrated with a standard α-Fe foil at room temperature, and all isomer shift values are referenced to α-Fe at 300 K. The spectral data were analyzed using the RECOIL package.[21] Static magnetic properties were investigated over a temperature range of 10–300 K and in applied magnetic fields up to 3 T using a Vibrating Sample Magnetometer (VSM) integrated into a Quantum Design Physical Property Measurement System (PPMS).

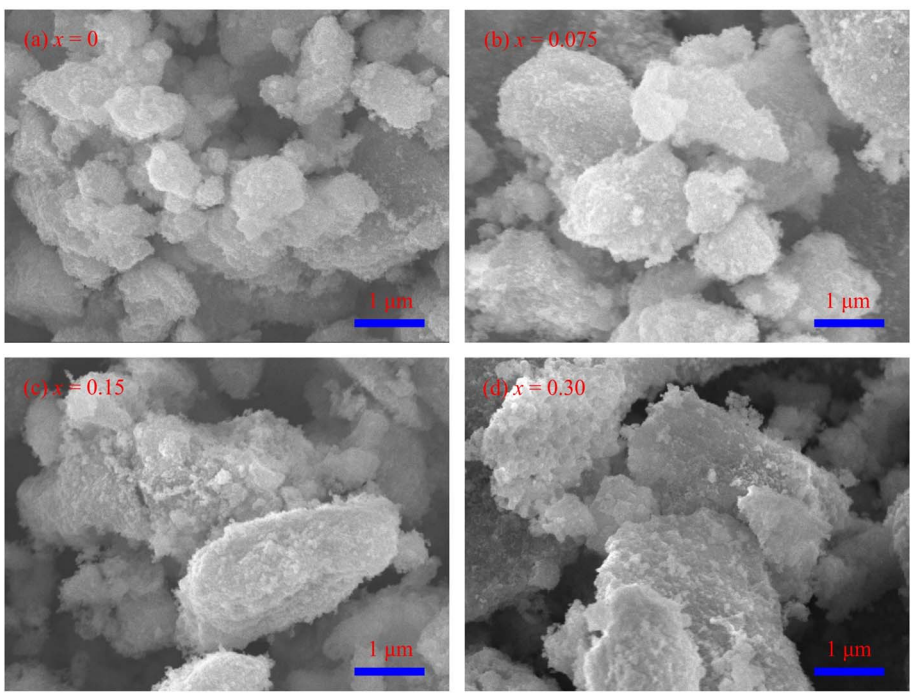

Fig. 1 SEM images of $Fe_{3-x}Lu_xO_4$ nanoparticles with $x = 0$ (a), 0.075 (b), 0.150 (c), and 0.3 (d).

III. Results and discussion

Elemental composition analysis by EDX confirms the presence of all constituent elements in the synthesized samples (Fig. S1), with their contents summarized in Table S1. The measured Lu-to-Fe atomic ratios are close to the expected values within the instrumental accuracy, as shown in Table S1. The morphological properties of the synthesized $Fe_{3-x}Lu_xO_4$ samples were investigated by SEM and TEM, as shown in Fig. 1 and 2, respectively. The SEM micrographs reveal irregularly shaped nanoparticles with a broad size distribution that tend to agglomerate into large clusters. Such agglomeration is commonly attributed to magnetic dipole–dipole and electrostatic interactions among ferrite nanoparticles.[12,22] As shown in Fig. 1, Lu substitution does not produce a clearly distinguishable change in particle size at the SEM scale, although a slight increase in nanoparticle agglomeration is observed with increasing Lu content. The TEM images further confirm the nanoscale nature of the $Fe_{3-x}Lu_xO_4$ particles. The pristine sample consists predominantly of nearly spherical particles with a broad size distribution, whereas Lu doping promotes the formation of particles with a more cubic morphology. The particle-size distributions of the synthesized samples were determined from TEM images using the open-source ImageJ software[23] and are presented in Fig. S2 of the SI. The average particle size tends to increase with Lu content, from ~15.6 nm for $x = 0$ to 44.7 nm for $x = 0.30$ (Fig. S2), suggesting gradual particle growth upon Lu substitution.

The crystalline properties of the synthesized samples were investigated using a combination of XRD (Fig. 3a) and NPD (Fig. 3b) techniques. As shown in Fig. 3a, all samples exhibit similar XRD patterns, corresponding to the single-phase cubic spinel structure of the $Fd\bar{3}m$ space group, with no detectable impurity peaks. The lattice constant increases gradually with increasing Lu concentration (Fig. 4a), which can be attributed to the larger ionic radius of Lu^{3+} (~0.861 Å) compared with that of Fe^{3+} (~0.645 Å) at the octahedral B sites. It should be noted that the preferential occupation of Lu^{3+} ions at the B sites cannot be reliably established from the present diffraction data alone; this assignment is further supported by the Mössbauer spectroscopy results discussed below. Moreover, the NPD patterns reveal additional magnetic contributions to the intensities of the (111) reflection at $d \approx 4.83$ Å, (220) at $d \approx 2.95$ Å, (222) at $d \approx 2.41$ Å and (400) at $d \approx 2.09$ Å (Fig. 3b), evidencing the presence of long-range ferrimagnetic ordering. The refined lattice parameters, atomic positions, ordered magnetic moments, and quality-of-fit factors obtained for the $Fe_{3-x}Lu_xO_4$ nanoparticles are summarized in Table 1. The refined ordered magnetic moments

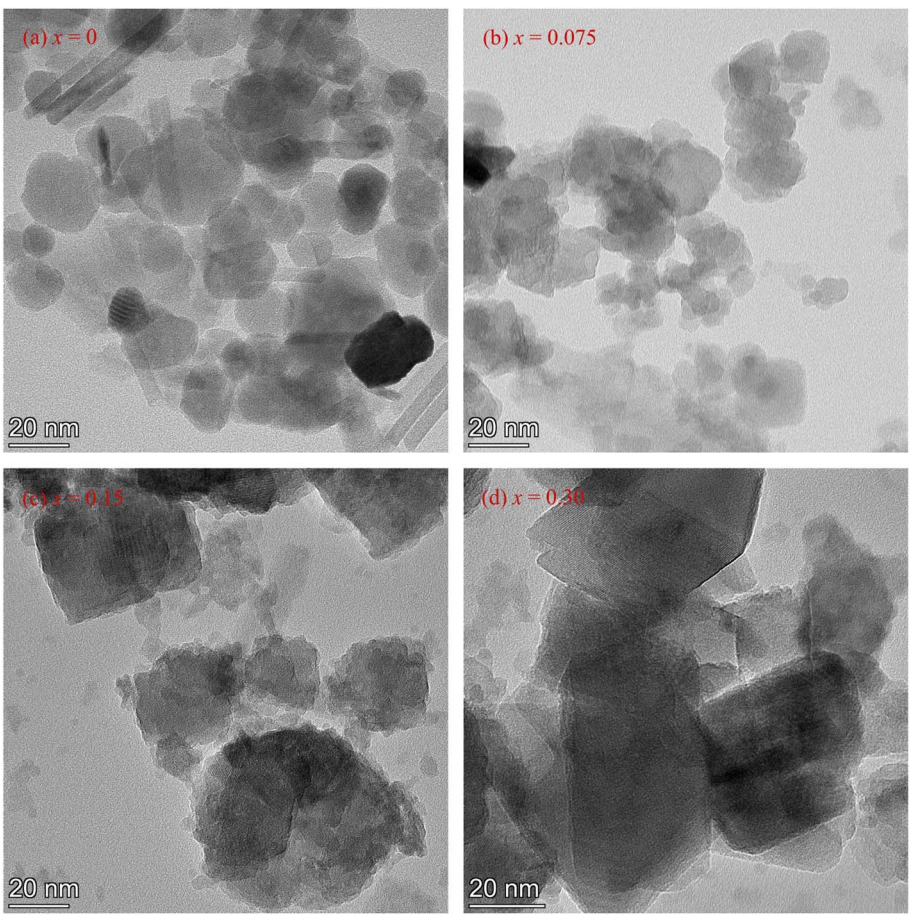

Fig. 2 TEM images of $Fe_{3-x}Lu_xO_4$ nanoparticles with $x = 0$ (a), 0.075 (b), 0.150 (c), and 0.3 (d).

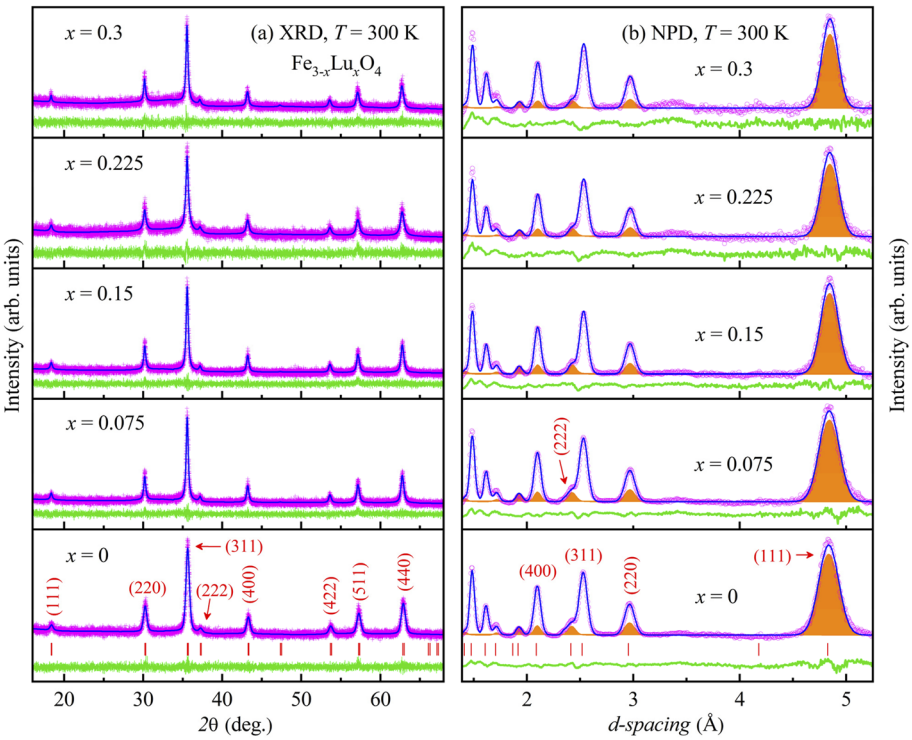

Fig. 3 Room-temperature XRD (a) and NPD (b) patterns (symbols) of $Fe_{3-x}Lu_xO_4$ nanoparticles together with the calculated refinement profiles. Tick marks indicate the calculated positions of the nuclear Bragg reflections corresponding to the cubic spinel structure, while the indices of characteristic reflections are labeled. The magnetic contribution to the NPD pattern is highlighted in orange in panel (b).

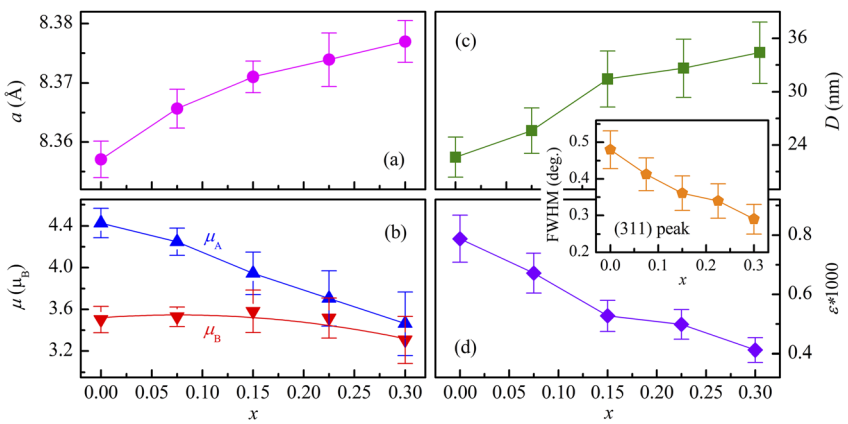

Fig. 4 Lattice parameters (a), ordered magnetic moments at the A and B sites (b), crystallite size D (c), and microstrain (d) of $Fe_{3-x}Lu_xO_4$ nanoparticles as a function of Lu doping concentration.

of the A and B sublattices for the pristine Fe_3O_4 are 4.43(14) μ_B and 3.50(13) μ_B, respectively, in good agreement with previously reported values.[24] Upon Lu substitution, the ordered magnetic moment of the A sublattice is significantly reduced, reaching 3.46(30) μ_B, whereas the magnetic moment of the B sublattice shows only a slight variation (Fig. 4b). The pronounced suppression of the coherent A-site magnetic moment is directly associated with the enhanced superparamagnetic relaxation revealed by Mössbauer spectroscopy. The incorporation of Lu^{3+} at the B sites disrupts a significant number of J_{AB} superexchange pathways, thereby magnetically isolating the A-site Fe^{3+} ions. In contrast, the Mössbauer spectral area associated with the B-site components remains nearly unchanged, indicating that the B sublattice largely remains in a magnetically blocked state.

Moreover, the crystallite size D and internal lattice strain ε were estimated from the XRD peak broadening using the Williamson–Hall (W–H) method.[25,26] Within the uniform deformation model, which assumes isotropic strain in all crystallographic directions,[25,26] the total peak broadening β_{hkl}, after subtracting the instrumental contribution, consists of size

Table 1 Room-temperature crystallographic characteristics of $Fe_{3-x}Lu_xO_4$ nanoparticles refined from neutron diffraction data. In the $Fd\bar{3}m$ crystal structure, the tetrahedral A and octahedral B cation sites correspond to the 8*a* (1/8, 1/8, 1/8) and 16*d* (1/2, 1/2, 1/2) Wyckoff positions, respectively, while oxygen atoms occupy the 32*e* (x_O, x_O, x_O) positions

x	0	0.075	0.15	0.225	0.30
Symmetry	$Fd\bar{3}m$	$Fd\bar{3}m$	$Fd\bar{3}m$	$Fd\bar{3}m$	$Fd\bar{3}m$
a (Å)	8.3571(31)	8.3657(33)	8.3710(27)	8.3739(45)	8.3770(35)
x_O	0.2585(6)	0.2590(6)	0.2595(9)	0.2615(11)	0.2626(12)
μ_A (μ_B)	4.43(14)	4.25(13)	3.95(20)	3.70(27)	3.46(30)
μ_B (μ_B)	3.50(13)	3.53(9)	3.58(20)	3.52(19)	3.31(22)
R_B (%)	3.29	3.27	4.59	8.54	9.81
R_p (%)	2.74	3.51	4.59	8.15	8.06
R_M (%)	4.03	3.45	4.78	5.89	3.79
χ^2	0.77	0.67	0.61	0.44	0.42

and strain contributions. Accordingly, the broadening of a reflection at θ_{hkl} can be expressed as: $\beta_D = \frac{K\lambda}{D\cos(\theta_{hkl})}$ and $\beta_\varepsilon = 4\varepsilon\tan(\theta_{hkl})$, where K and λ are the shape factor and X-ray wavelength, respectively. By plotting $\beta_{hkl}\cos(\theta_{hkl})$ *versus* $4\sin(\theta_{hkl})$, as shown in Fig. S3, a linear fit to the data allows for the extraction of the microstrain ε from the slope and the crystallite size D from the y-intercept.

As shown in Fig. 4c and d, the crystallite size increases from 22.6(2) to 34.4(2) nm with increasing Lu concentration, consistent with the aforementioned morphological results, while the microstrain decreases from $0.78(8) \times 10^{-3}$ for $x = 0$ to $0.41(4) \times 10^{-3}$ at $x = 0.30$. The increase in D is further evidenced by the progressive narrowing of the (311) diffraction peak with increasing Lu content, as shown in the inset of Fig. 4. This structural coarsening is attributed to modified nucleation and growth kinetics driven by Lu^{3+} incorporation during the co-precipitation process. Specifically, the substitution of Fe^{3+} by the larger Lu^{3+} ions induces significant local lattice distortion at the octahedral sites of the spinel structure. To minimize the resultant strain energy, the system promotes the growth of larger crystallites, likely through defect-assisted Ostwald ripening.[27] Furthermore, the presence of Lu^{3+} may alter the precursor solubility and reduce the local supersaturation during the addition of NH_4OH, thereby suppressing the initial nucleation rate.[28] A lower density of primary nuclei facilitates continued solute deposition onto existing particles, promoting nanoparticle coarsening.[28] Consequently, the observed reduction in microstrain signifies effective structural relaxation and improved crystalline ordering at higher Lu concentrations.

To gain insights into the effect of Lu^{3+} substitution on the magnetic relaxation and local exchange interactions in $Fe_{3-x}Lu_xO_4$ nanoparticles, ^{57}Fe Mössbauer spectra were recorded at room temperature and 20 K for selected samples, as depicted in Fig. 5. As shown in Fig. 5a, the room-temperature Mössbauer spectrum of pristine Fe_3O_4 can be deconvoluted into a broadened singlet (S) and three distinct magnetic sextets (H_1, H_2, and H_3). The singlet S, accounting for 8.0% of the total spectral area with a remarkably broad linewidth, indicates the presence of ultrafine nanoparticles undergoing fast superparamagnetic relaxation due to their low magnetic anisotropy energy barrier. The sextet H_1, exhibiting the highest hyperfine field of 49.1 T, is assigned to high-spin Fe^{3+} ions at tetrahedral A-sites. In contrast, the H_2 and H_3 sextets correspond to Fe ions located at octahedral B-sites. Since 300 K is well above the Verwey transition temperature, rapid electron hopping occurs between Fe^{2+} and Fe^{3+} ions in the B-sublattice.[29–31] Because the hopping frequency exceeds the Mössbauer timescale, the ^{57}Fe nuclei experience a time-averaged environment corresponding to an intermediate $Fe^{2.5+}$ valence state.[29–31] This electron delocalization phenomenon reduces the internal magnetic field, explaining the lower H_{eff} values of the B-site components compared with the A-site component. Accordingly, H_2 (H_{eff} = 47.0 T) is attributed to $Fe^{2.5+}$ ions in the well-ordered nanoparticle core.[29–31] The H_3 sextet exhibits a significantly reduced hyperfine field of 41.9 T together with a broadened linewidth (Γ = 0.403 mm s^{-1}), suggesting the presence of $Fe^{2.5+}$ ions located in a non-stoichiometric environment, such as the nanoparticle surface or regions adjacent to cation vacancies, where the partial disruption of the J_{AB} superexchange pathways leads to weakened magnetic coupling and a broader distribution of local magnetic fields.

Upon Lu^{3+} substitution, the superparamagnetic fraction increases dramatically to 26.0% and 24.0% for $x = 0.15$ and 0.30, respectively (see left panels of Fig. 5 and Table 2). This substantial increase is accompanied by a corresponding reduction of the H_1 spectral area, which decreases by 19.6% and 19.2% for $x = 0.15$ and 0.30, respectively, relative to pristine Fe_3O_4. In contrast, the total spectral contribution of the B-site components (H_2 + H_3) remains nearly unchanged, varying only slightly between 47.5% and 50.7% across all samples. These results indicate that the enhanced superparamagnetism mainly originates from the destabilization of A-site Fe^{3+} ions. At the same time, the H_2 fraction shows only a slight decrease, whereas the H_3 component progressively increases with Lu concentration, reaching +1.8% at $x = 0.15$ and +4.7% at $x = 0.30$ compared with pristine Fe_3O_4. This systematic enhancement of the H_3 contribution provides strong evidence that Lu^{3+} incorporation promotes the formation of defective and non-stoichiometric regions within the spinel lattice. Moreover, Lu^{3+} substitution induces an anisotropic suppression of H_{eff} among the different crystallographic sites. Whereas the A-site component (H_1) exhibits only a moderate reduction of ~1.8–2.5 T, the B-site components are much more strongly affected. In particular, the ordered B-site component (H_2) decreases by ~3.6–4.8 T, while the defective B-site contribution (H_3) undergoes the strongest collapse, dropping by ~5.7–7.2 T.

As shown below, Lu^{3+} ions preferentially occupy the octahedral B-sites, thereby directly perturbing the local electronic and magnetic environment of the B-sublattice. The drastic reduction of the H_1 spectral area suggests that A-site Fe^{3+} ions surrounded by diamagnetic Lu^{3+} neighbors lose a critical number of J_{AB} superexchange pathways, causing their anisotropy energy to become sufficiently weak for thermal fluctuations at 300 K to average out the magnetic splitting into the singlet S component. Consequently, the remaining H_1 sextet

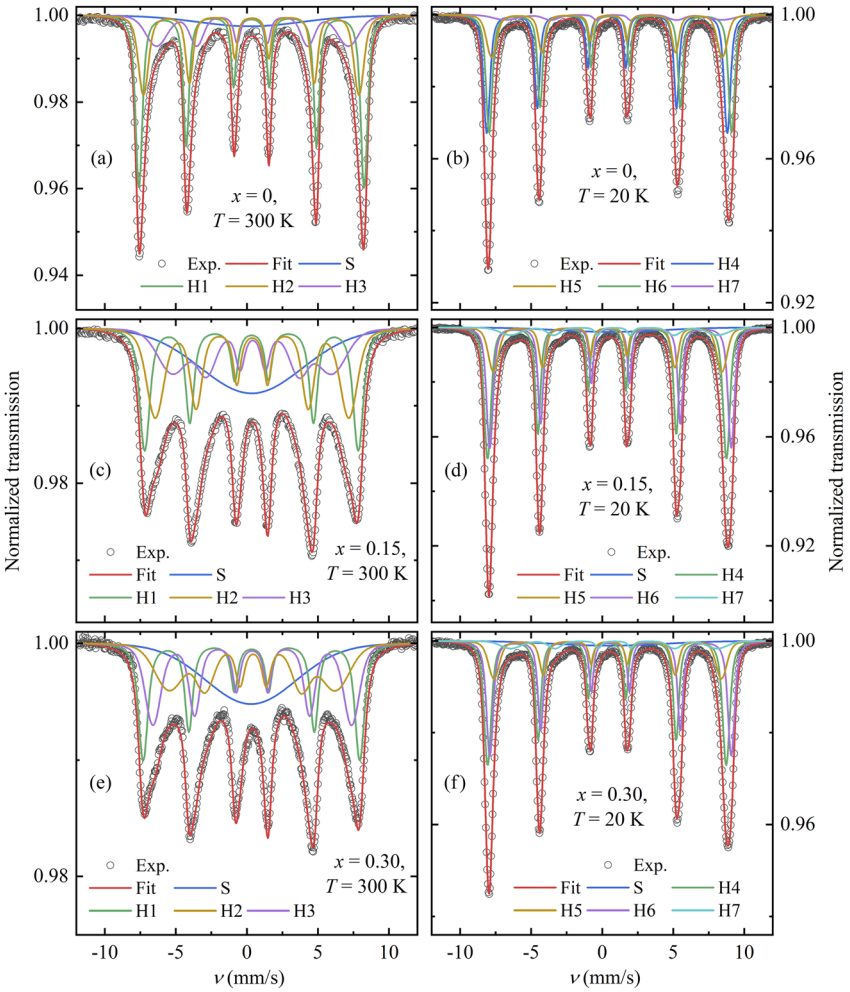

Fig. 5 Mössbauer spectra of $Fe_{3-x}Lu_xO_4$ nanoferrites measured at 300 K (a, c and e – left) and 20 K (b, d and f – right).

mainly originates from Fe^{3+} ions located in relatively intact Lu-poor environments, where the local magnetic coordination remains largely preserved and H_{eff} remains only weakly suppressed. In contrast, the strong H_{eff} reduction observed for the B-site components (H_2 and H_3), despite their relatively preserved spectral areas, mainly arises from the disruption of the $Fe^{2+} \leftrightarrow Fe^{3+}$ electron-hopping network together with local lattice distortions, both of which intrinsically reduce the time-averaged internal magnetic field throughout the octahedral sublattice.

At 20 K, well below the Verwey transition temperature, electron hopping becomes frozen, resulting in clear separation of the Mössbauer spectrum into three distinct components associated with Fe^{3+} at A-sites, Fe^{3+} at B-sites, and Fe^{2+} at B-sites (right panels of Fig. 5). The low-temperature spectra provide direct evidence for preferential Lu^{3+} occupation at octahedral B-sites. With increasing Lu concentration, the spectral areas of the B-site components H_5 (Fe^{3+}) and H_6 (Fe^{2+}) decrease, whereas the A-sites component H_4 slightly increases. In addition, the appearance of the H_7 sextet with a relatively large isomer shift (δ > 0.8 mm s^{-1}) indicates significant local distortion of the octahedral environment induced by the larger Lu^{3+} ions.

The refined hyperfine parameters at 20 K further demonstrate progressive magnetic disordering upon Lu substitution (Table 2). Although the isomer shift remains nearly unchanged, indicating preservation of the Fe valence states, H_{eff} systematically decreases for all subspectra. The strongest reduction occurs for the H_7 component, assigned to Fe^{2+} ions at distorted octahedral B-sites, where H_{eff} decreases from 47.2 T in pristine Fe_3O_4 to 45.0 T for $x = 0.30$. This behavior reflects weakening of the J_{AB} superexchange interactions and increasing magnetic disorder, consistent with the magnetometry results. Notably, at 20 K, the superparamagnetic singlet component completely disappears in pristine Fe_3O_4, indicating the suppression of superparamagnetic relaxation below the blocking regime. In contrast, the Lu-substituted samples retain a residual singlet contribution of ~4%, evidencing the persistence of magnetically disordered or slowly relaxing regions even at low temperature. Slight broadening of the sextet linewidths further supports enhanced local structural and magnetic inhomogeneity induced by Lu^{3+} substitution. Although the physical crystallite size increases with Lu content, the substitution of non-magnetic Lu^{3+} ions at the octahedral B-sites weakens the dominant J_{AB} superexchange interactions and introduces local

Table 2 Hyperfine parameters determined from the ^{57}Fe Mössbauer spectra of $Fe_{3-x}Lu_xO_4$ nanoferrites. The parameter designations are as follows: δ – isomer shift, Δ – quadrupole splitting, H_{eff} – effective magnetic field on ^{57}Fe nuclei, Γ – line width, I – relative intensity. Component labels: S – broad singlet; H – sextet; D – doublet

x, T	Comp.	δ (mm s^{-1})	Δ (mm s^{-1})	H_{eff} (T)	Γ (mm s^{-1})	I (%)	Assignment
$x = 0$, 300 K	S	0.21(2)	—	—	7.222(5)	8.0(1)	SP/Fe_3O_4
	H_1	0.33(2)	0.00(2)	49.1(5)	0.222(5)	44.5(1)	Fe^{3+}/Fe_3O_4(A)
	H_2	0.33(2)	−0.02(2)	47.0(5)	0.256(5)	27.6(1)	$Fe^{2.5+}$/Fe_3O_4(B)
	H_3	0.39(2)	0.01(2)	41.9(5)	0.403(5)	19.9(1)	$Fe^{2.5+}$/Fe_3O_4(B)
$x = 0.15$, 300 K	S	0.34(2)	—	—	7.151(5)	26.0(1)	SP/Fe_3O_4
	H_1	0.33(2)	−0.01(2)	46.6(5)	0.322(5)	24.9(1)	Fe^{3+}/Fe_3O_4(A)
	H_2	0.37(2)	−0.01(2)	42.2(5)	0.400(5)	27.4(1)	$Fe^{2.5+}$/Fe_3O_4(B)
	H_3	0.39(2)	−0.02(2)	34.7(5)	0.568(5)	21.7(1)	$Fe^{2.5+}$/Fe_3O_4(B)
$x = 0.3$, 300 K	S	0.31(2)	—	—	6.309(5)	24.0(1)	SP/Fe_3O_4
	H_1	0.33(2)	0.00(2)	47.3(5)	0.313(5)	25.3(1)	Fe^{3+}/Fe_3O_4(A)
	H_2	0.38(2)	0.01(2)	43.4(5)	0.380(5)	26.1(1)	$Fe^{2.5+}$/Fe_3O_4(B)
	H_3	0.41(2)	−0.03(2)	36.2(5)	0.555(5)	24.6(1)	$Fe^{2.5+}$/Fe_3O_4(B)
$x = 0$, 20 K	H_4	0.33(2)	0.01(2)	52.5(5)	0.192(5)	38.1(1)	Fe^{3+}/Fe_3O_4(A)
	H_5	0.40(2)	−0.06(2)	50.3(5)	0.234(5)	19.5(1)	Fe^{3+}/Fe_3O_4(B)
	H_6	0.57(2)	0.01(2)	52.9(5)	0.191(5)	37.1(1)	Fe^{2+}/Fe_3O_4(B)
	H_7	0.82(2)	0.01(2)	47.2(5)	0.449(5)	5.3(1)	Fe^{2+}/Fe_3O_4(B)
$x = 0.15$, 20 K	S	0.58(2)	—	—	7.240(5)	3.9(1)	SP
	H_4	0.34(2)	0.00(2)	52.1(5)	0.191(5)	38.4(1)	Fe^{3+}/Fe_3O_4(A)
	H_5	0.42(2)	−0.04(2)	49.9(5)	0.231(5)	18.0(1)	Fe^{3+}/Fe_3O_4(B)
	H_6	0.58(2)	0.00(2)	52.7(5)	0.190(5)	34.0(1)	Fe^{2+}/Fe_3O_4(B)
	H_7	0.84(2)	0.01(2)	45.3(5)	0.380(5)	5.7(1)	Fe^{2+}/Fe_3O_4(B)
$x = 0.3$, 20 K	S	0.50(2)	—	—	7.601(5)	4.4(1)	SP
	H_4	0.34(2)	−0.01(2)	52.0(5)	0.210(5)	39.0(1)	Fe^{3+}/Fe_3O_4(A)
	H_6	0.44(2)	−0.06(2)	49.6(5)	0.253(5)	16.5(1)	Fe^{3+}/Fe_3O_4(B)
	H_5	0.58(2)	0.00(2)	52.7(5)	0.206(5)	34.4(1)	Fe^{2+}/Fe_3O_4(B)
	H_7	0.86(2)	−0.03(2)	45.0(5)	0.373(5)	5.7(1)	Fe^{2+}/Fe_3O_4(B)

exchange disorder. This magnetic dilution may disrupt the continuity of the ferrimagnetic network and promote the formation of smaller, weakly coupled Fe-containing magnetic regions within individual nanoparticles. The pronounced increase in the area of the singlet at 300 K is therefore attributed predominantly to the rapid superparamagnetic relaxation of these weakly correlated regions. This interpretation is supported by the Mössbauer spectra recorded at 20 K, where the reduction in thermal energy increases the magnetic relaxation time and blocks the corresponding moments on the Mössbauer timescale, causing the singlet component to nearly disappear and magnetically split sextets to emerge.

Furthermore, the Lu doping effect on the magnetic properties of $Fe_{3-x}Lu_xO_4$ nanoferrites was investigated through $M(H)$ measurements. Fig. 6 presents the $M(H)$ loops (−30 to 30 kOe) of the $Fe_{3-x}Lu_xO_4$ samples measured at 10, 50, 100, 150, 200, 250, 300, and 350 K. The extracted parameters, coercivity (H_c) and remanent magnetization (M_r), are summarized in Table 3. At low temperatures, all samples exhibit pronounced ferrimagnetic hysteresis associated with thermally blocked magnetic moments. As the temperature approaches room temperature, the pristine and lightly Lu-substituted samples evolve toward a nearly superparamagnetic response on the DC magnetometry timescale, as evidenced by the pronounced reduction in coercivity and remanence. This behavior is attributed to their smaller particle sizes, which enable a larger fraction of nanoparticles to overcome the blocking condition at elevated temperatures. In contrast, the finite hysteresis retained by the more highly substituted samples indicates the coexistence of blocked ferrimagnetic particles and superparamagnetically relaxing fractions arising from the broad particle size distribution. A systematic decrease in the maximum magnetization (M_{max}) with increasing Lu^{3+} concentration is observed. This behavior is expected, as the substitution of non-magnetic Lu^{3+} for Fe^{3+} at the octahedral B sublattice reduces the sublattice magnetization difference ($M_B - M_A$), in accordance with the Goodenough–Kanamori–Anderson (GKA) superexchange framework.[32] Additionally, the much larger ionic radius of Lu^{3+} introduces local lattice distortion that weakens the Fe–O–Fe J_{AB} exchange and enhances spin canting, thereby contributing to the reduction in the remanent magnetization.

In contrast, the coercive field (H_c) increases monotonically with Lu incorporation. This enhancement originates from strain-induced anisotropy, increased exchange inhomogeneity, and the formation of local pinning centers that inhibit domain-wall motion.[33,34] For the present nanoparticle system, surface anisotropy and dipolar interactions also play a dominant role in determining H_c, as further discussed below. Notably, the data in Table 3 show that the undoped sample ($x = 0$) exhibits a pronounced reduction of macroscopic hysteresis at 300 K, with $H_c = 4.44$ Oe and $M_r/M_s = 0.009$. When considered together with the substantially larger coercivity observed at 10 K ($H_c = 191.67$ Oe), the temperature dependence described by Kneller's relation, and the presence of a Mössbauer singlet at room temperature, this behavior is consistent with thermally activated unblocking and a crossover toward a nearly

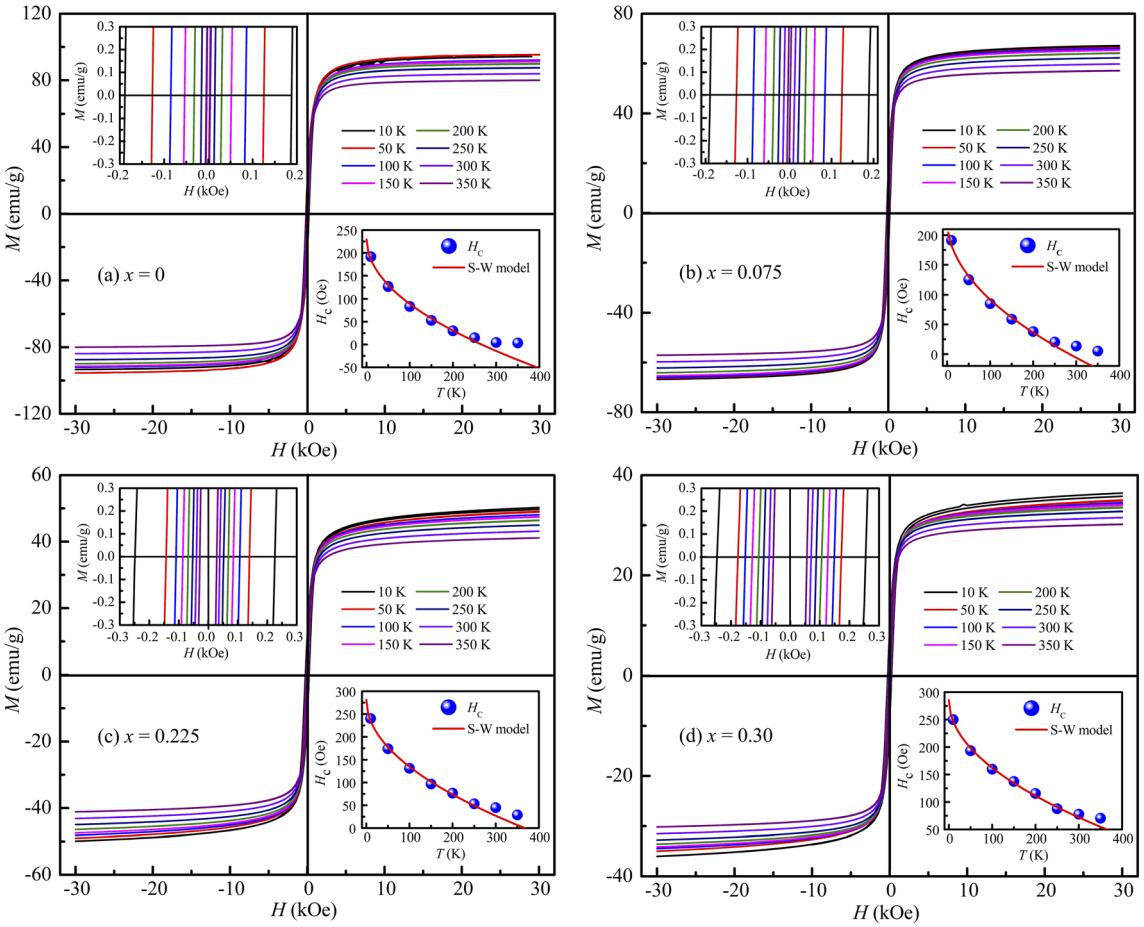

Fig. 6 Magnetic hysteresis loops $M(H)$ measured between −30 and 30 kOe at various temperatures for the $Fe_{3-x}Lu_xO_4$ nanoferrites. The upper-left insets in panels (a–d) show enlarged views of the low-field region used to extract the coercive field (H_c). The lower-right inset presents the temperature dependence of H_c together with the corresponding fit using the Kneller model.

superparamagnetic regime on the DC magnetometry timescale. A similar thermally driven evolution is observed for the $x = 0.075$ sample at 350 K ($H_c = 5.05$ Oe, $M_r/M_s = 0.008$). This interpretation does not imply that the entire nanoparticle ensemble becomes fully superparamagnetic; rather, it indicates that a significant fraction of nanoparticles undergoes thermally activated relaxation within the DC measurement window.

Overall, the concurrent suppression of M_{max} and M_r, accompanied by the increase in H_c, demonstrates that Lu doping markedly modifies both the exchange interactions and anisotropy field of the $Fe_{3-x}Lu_xO_4$ nanoferrites. The temperature dependence of H_c for $Fe_{3-x}Lu_xO_4$ samples (10–250 K) was analyzed using Kneller's law, $H_c = H_{c0}[1 - (T/T_B)^{1/2}]$,[35] where H_{c0} and T_B are the zero-temperature coercivity and blocking temperature, respectively. Fitting yields $H_{c0} = 229.8$–285.7 Oe and $T_B = 266.2$–535.9 K, increasing with Lu content (Table 4). For non-interacting spherical particles, the effective anisotropy constant (K_{eff}) is given by $H_c = 0.64K_{eff}/M_s$, resulting in K_{eff} values up to 1.46×10^5 erg cm^{-3} at 10 K for $x = 0$, roughly one order of magnitude lower than that of Fe_3O_4 nanoparticles (5.9×10^6 erg cm^{-3} at 5 K (ref. 36)). K_{eff} decreases monotonically with both temperature and Lu^{3+} concentration. This reduction is attributed to surface spin disorder and canting, weakening of J_{AB} superexchange by non-magnetic Lu^{3+} substitution, and lattice distortions induced by the larger ionic radius of Lu^{3+}. Together, these effects explain the observed variation of H_c and K_{eff}, highlighting the combined influence of nanoscale effects and doping on the magnetic anisotropy of $Fe_{3-x}Lu_xO_4$ nanoferrites.

To accurately determine the saturation magnetization (M_s) and the magnetocrystalline anisotropy constant (K_1), the initial magnetization curves were analyzed using the Law of Approach to Saturation (LAS). The LAS expression,[37,38]

$$M(H) = M_s\left(1 - \frac{a}{H} - \frac{b}{H^2}\right) + \chi_d H, \quad (1)$$

accounts for spin deviation near saturation, where the term a/H reflects microstructural inhomogeneity (negligible at high fields), and b/H^2 dominates in the high-field regime and is related to anisotropy through the following equation:[37,38]

$$b = \frac{8{K_1}^2}{105{M_s}^2}. \quad (2)$$

Reliable convergence of the LAS fitting was achieved by minimizing the sum of squared residuals (SSR) while selectively

Table 3 Saturation magnetization (M_s), remanent magnetization (M_r), coercivity (H_c), first-order cubic anisotropy constant (K_1) and squareness ratio (M_r/M_s) at various temperature of $Fe_{3-x}Lu_xO_4$ nanoparticles

Sample	Temp. (K)	M_s (emu g^{-1})	M_s (μ_B)	M_r (emu g^{-1})	H_c (Oe)	M_r/M_s	$b \times 10^6$ (Oe^2)	$K_1 \times 10^6$ (erg cm^{-3})
$x = 0$	10	92.48	3.83	22.39	191.67	0.24	1.26	2.05
	55	93.29	3.87	16.42	126.66	0.18	1.28	2.08
	100	90.92	3.77	10.88	83.33	0.12	1.24	2.00
	150	89.41	3.71	7.48	52.77	0.08	1.18	1.92
	200	88.12	3.65	4.67	30.13	0.05	1.13	1.85
	250	85.19	3.53	2.42	14.96	0.03	1.05	1.72
	300	82.68	3.43	0.77	4.44	0.009	0.94	1.58
	350	78.81	3.27	0.69	3.45	0.009	0.83	1.42
$x = 0.075$	10	64.86	2.79	16.272	191.10	0.25	1.20	1.37
	55	64.26	2.77	11.376	125.01	0.18	1.22	1.37
	100	63.40	2.73	8.2196	85.01	0.13	1.17	1.32
	150	62.87	2.71	6.036	58.81	0.10	1.15	1.30
	200	61.80	2.66	4.0909	37.90	0.07	1.12	1.26
	250	59.19	2.55	2.6545	20.33	0.04	1.06	1.18
	300	57.96	2.50	1.522	13.54	0.03	1.01	1.12
	350	55.41	2.39	0.456	5.05	0.008	0.93	1.03
$x = 0.225$	10	46.36	2.14	12.21	240.20	0.26	1.57	1.15
	55	45.95	2.13	8.64	144.02	0.19	1.55	1.13
	100	45.12	2.09	6.82	111.04	0.15	1.51	1.09
	150	44.03	2.04	5.67	86.63	0.13	1.49	1.06
	200	43.28	2.00	4.72	66.60	0.11	1.41	1.01
	250	42.19	1.95	3.81	53.31	0.09	1.35	0.97
	300	40.72	1.88	2.97	38.80	0.07	1.32	0.92
	350	39.05	1.81	2.29	28.88	0.06	1.23	0.85
$x = 0.30$	10	33.09	1.58	8.82	249.99	0.27	1.37	0.77
	55	32.96	1.58	7.02	173.35	0.21	1.36	0.77
	100	32.47	1.55	6.16	149.71	0.19	1.26	0.73
	150	31.89	1.53	5.51	127.31	0.17	1.23	0.71
	200	31.18	1.49	4.83	105.55	0.15	1.20	0.68
	250	30.68	1.47	4.17	87.73	0.14	1.15	0.65
	300	29.85	1.43	3.62	70.80	0.12	1.10	0.62
	350	28.79	1.38	3.15	57.50	0.11	1.06	0.59

Table 4 Effective anisotropy constant (K_{eff}), maximum dipolar field (H_{dip}) and magnetic grain size (D_m) at various temperature for $Fe_{3-x}Lu_xO_4$ nanoparticles

Temp. (K)		10	50	100	150	200	250	300	350
$x = 0$	$K_{eff} \times 10^4$ (erg cm^{-3})	14.59	9.73	6.24	3.88	2.19	1.05	0.30	0.22
	H_{dip} (kOe)	11.78	17.83	27.10	42.79	74.93	150.88	508.20	654.86
	D_m (nm)	22.91	26.23	30.41	35.62	43.14	55.09	83.41	92.23
$x = 0.075$	$K_{eff} \times 10^4$ (erg cm^{-3})	10.31	6.70	4.48	3.07	1.95	1.00	0.65	0.23
	H_{dip} (kOe)	12.49	19.10	28.09	40.60	62.99	117.44	176.33	472.79
	D_m (nm)	26.30	30.39	34.71	39.38	45.82	57.22	65.98	93.04
$x = 0.225$	$K_{eff} \times 10^4$ (erg cm^{-3})	9.46	5.62	4.26	3.24	2.45	1.91	1.34	0.96
	H_{dip} (kOe)	12.56	20.95	27.18	34.82	45.29	56.59	77.75	104.45
	D_m (nm)	29.46	35.04	38.45	42.11	46.23	50.22	56.49	63.20
$x = 0.30$	$K_{eff} \times 10^4$ (erg cm^{-3})	7.11	4.91	4.18	3.49	2.83	2.31	1.82	1.42
	H_{dip} (kOe)	17.41	25.11	29.08	34.20	41.24	49.62	61.49	75.71
	D_m (nm)	36.76	41.59	43.89	46.61	49.98	53.45	57.94	62.85

varying b and M_s in the high-field region (H > 1.0 T). Fig. 7 presents the experimental $M(H)$ curves together with the LAS fits, and the optimized values of b and M_s at each temperature for studied samples are listed in Table 3.

From Table 3, M_s of all samples increases monotonically with decreasing temperature, which reflects the progressive strengthening of magnetic exchange interactions and the corresponding suppression of long-wavelength spin-wave excitations at low temperatures. This behavior follows Bloch's $T^{3/2}$ law:[38,39]

$$M_s(T) = M_s(0)(1 - AT^{3/2}), \quad (3)$$

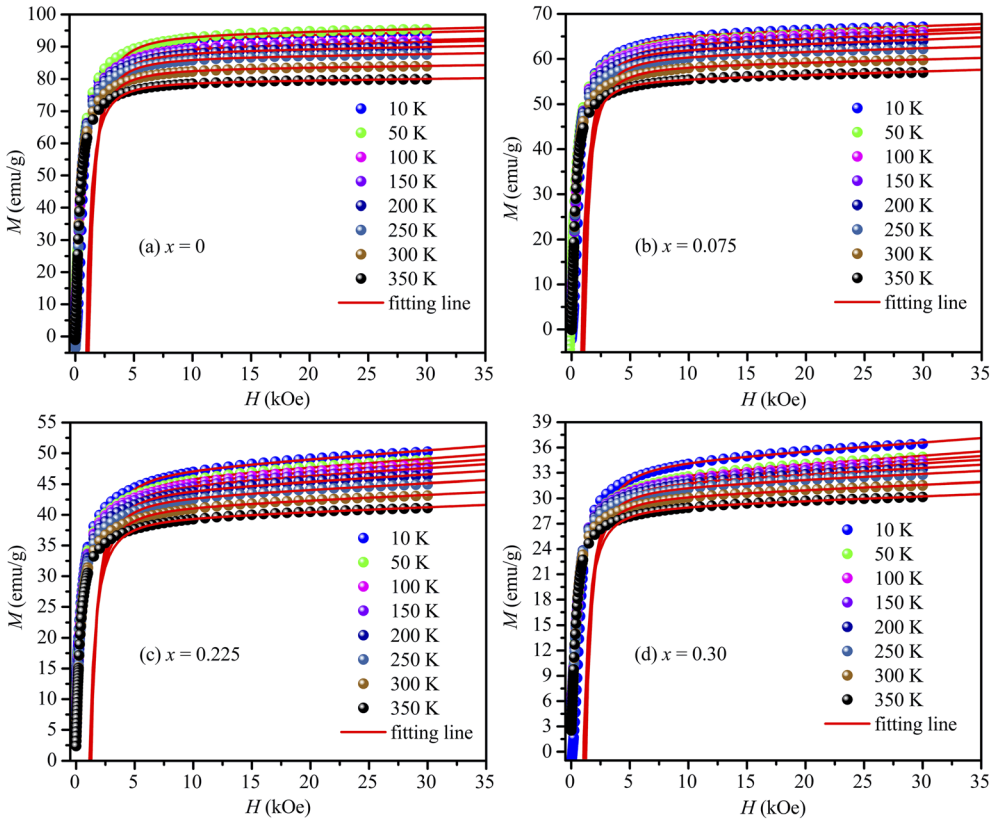

Fig. 7 Experimental and fitted magnetization curves for samples (a) $x = 0$, (b) $x = 0.075$, (c) $x = 0.225$, and (d) $x = 0.30$ at selected temperatures, modeled using the law of approach to saturation (LAS). Solid dots denote the measured M–H data, while solid lines represent the optimized LAS fits obtained by minimizing the sum of squared residuals.

where $M_s(0)$ is the extrapolated zero-temperature magnetization and A is the Bloch constant. As shown in Fig. 8, the experimental $M_s(T)$ data of all four samples agree well with this model. The inset of Fig. 8 further confirms the validity of the Bloch description by plotting $[M_s(0) - M_s(T)]/M_s(0)$ as a function of $T^{3/2}$. The extracted Bloch constants, $A \approx (1.96\text{–}2.36) \times 10^{-5}$, fall within the typical range reported for spinel ferrites,[40] reflecting their comparable exchange stiffness. The extrapolated values of $M_s(0)$ are 93.77 emu g^{-1} (3.89 μ_B), 65.07 emu g^{-1} (2.80 μ_B), 46.30 emu g^{-1} (2.14 μ_B), and 33.13 emu g^{-1} (1.59 μ_B) for $x = 0$, 0.075, 0.225 and 0.30, respectively. For the undoped sample ($x = 0$), the obtained moment is slightly lower than the theoretical value of 4 μ_B for ideal Fe_3O_4, likely due to a reduction in A–B superexchange strength, consistent with the Yafet–Kittel noncollinear spin-structure description,[41] together with surface spin disorder inherent to nanoparticles.

The magnetocrystalline anisotropy constant K_1 was evaluated by substituting the fitted parameters b and M_s into eqn (2). The resulting K_1 values across the investigated temperature range are summarized in Table 3. For all samples, K_1 decreases systematically with increasing Lu content and with increasing temperature. The thermal reduction of K_1 is consistent with the progressive weakening of spin–orbit coupling and the enhancement of thermal spin fluctuations. The compositional dependence can be rationalized by considering cation substitution at the octahedral (B) sublattice. Replacing magnetic Fe^{3+} ($3d^5$, high-spin) with nonmagnetic Lu^{3+} ($4f^{14}$, closed-shell) dilutes the anisotropic contribution arising from Fe–O–Fe superexchange interactions and suppresses the local spin–orbit-driven anisotropy at B sites. Moreover, Lu incorporation perturbs the local lattice environment and enhances structural disorder, further reducing both single-ion and magnetoelastic contributions to the anisotropy energy. These combined effects lead to the observed monotonic decrease of K_1 with Lu substitution.

The temperature dependence of H_c and K_{eff} in $Fe_{3-x}Lu_xO_4$ nanoparticles can be understood by considering both particle size and interparticle interactions. The low M_r/M_s ratios at various temperatures in Table 3 (<0.5) indicate magnetostatic (dipolar) interactions between particles dominate, rather than exchange coupling.[42] As Lu content increases, the particle volume (V_m) grows, leading to a decrease in $K_{eff} = 25k_BT_B/V_m$, despite the observed increase in H_c arising from strain-induced anisotropy and enhanced pinning. Therefore, the monotonic reduction of K_{eff} (see Table 4) with Lu concentration reflects the combined effects of larger particle size and dilution of the magnetic sublattice by non-magnetic Lu^{3+}, whereas H_c is primarily governed by surface and dipolar contributions rather than intrinsic anisotropy.[43]

The magnetic grain volume V_m was estimated from the blocking temperature using $T_B = K_{eff}V_m/25k_B$.[44] The corresponding magnetic grain diameters D_m at different

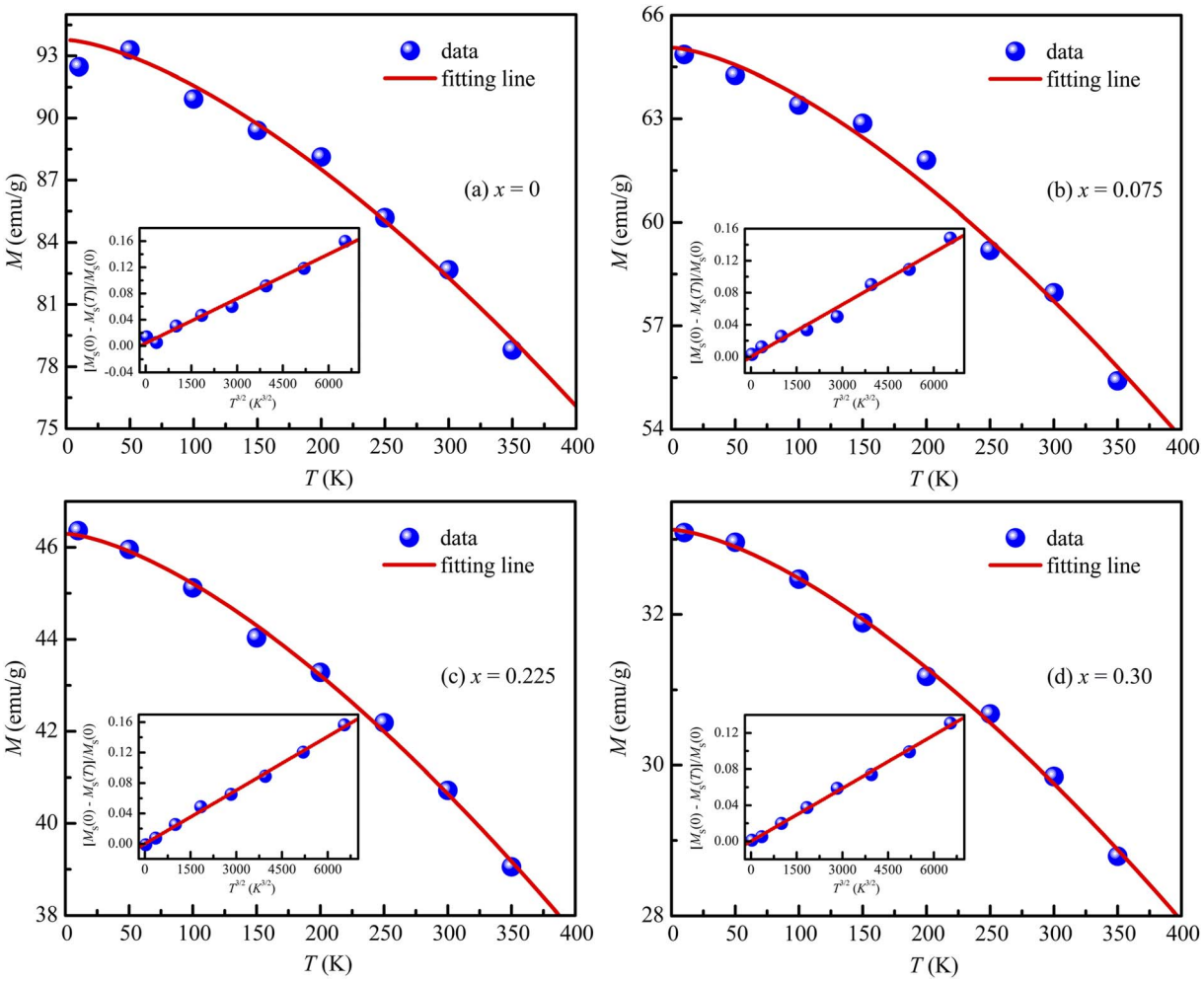

Fig. 8 Temperature dependence of the saturation magnetization $M_s(T)$ for samples with (a) $x = 0$, (b) $x = 0.075$, (c) $x = 0.225$, and (d) $x = 0.30$. The solid red lines represent the fits to Bloch's $T^{3/2}$ law. The insets display the reduced magnetization $[M_s(0) - M_s(T)]/M_s(0)$ plotted as a function of $T^{3/2}$, highlighting the contribution of spin-wave excitations.

temperatures are listed in Table 4. For all samples, D_m increases monotonically with temperature and remains larger than the TEM particle size, indicating collective magnetization behavior induced by dipolar interactions among neighboring grains.[33,34] These results confirm that the effective anisotropy arises from the combined contributions of magnetocrystalline anisotropy and surface-related dipolar effects. The dipolar interaction strength was further evaluated by the maximum dipolar field between nearest-neighbor grains, $H_{dip} = 2\mu/d^3$, where $\mu = M_s \times V_m$ is the particle magnetic moment and d is the interparticle separation.[45] The extracted H_{dip} values (Table 4) decrease systematically with increasing Lu content, consistent with the reduction in magnetic moment per grain and the dilution of the magnetic sublattice. Moreover, H_{dip} increases rapidly above 250 K due to the enlargement of D_m and thus μ at elevated temperatures.

Importantly, D_m for the undoped sample ($x = 0$) is smaller than that of the Lu-doped samples from 10 K to 250 K, indicating a larger surface-to-volume ratio and hence stronger surface anisotropy and enhanced dipolar coupling in this temperature range. At $T \geq 300$ K, the trend reverses and D_m becomes larger for $x = 0$, reflecting the reduced contribution of surface spins at elevated temperatures and the growing influence of thermally assisted dipolar correlations in the undoped material.

Fig. 9 displays the relationship between the magnetocrystalline anisotropy constant, $K_1(T)$, and the saturation magnetization, $M_s(T)$, analyzed within the Callen–Callen power-law framework. For all $Fe_{3-x}Lu_xO_4$ nanoparticles, the extracted scaling exponents q fall within the range 1.26–1.83, markedly lower than the theoretical values predicted for bulk systems with cubic symmetry (*e.g.*, $q = 6$ for uncorrelated and $q = 10$ for fully correlated moments).[46] The insets of Fig. 9 present linearized plots of $K_1(T)$ *versus* $M_s^q(T)$, confirming the corresponding q exponents for each composition.

Such pronounced deviations from the ideal Callen–Callen scaling arise because several key assumptions of the theory are not strictly fulfilled in nanoscale ferrites. In particular, spinel ferrites possess multiple magnetic sublattices, exchange–anisotropic interactions, and mixed origin of

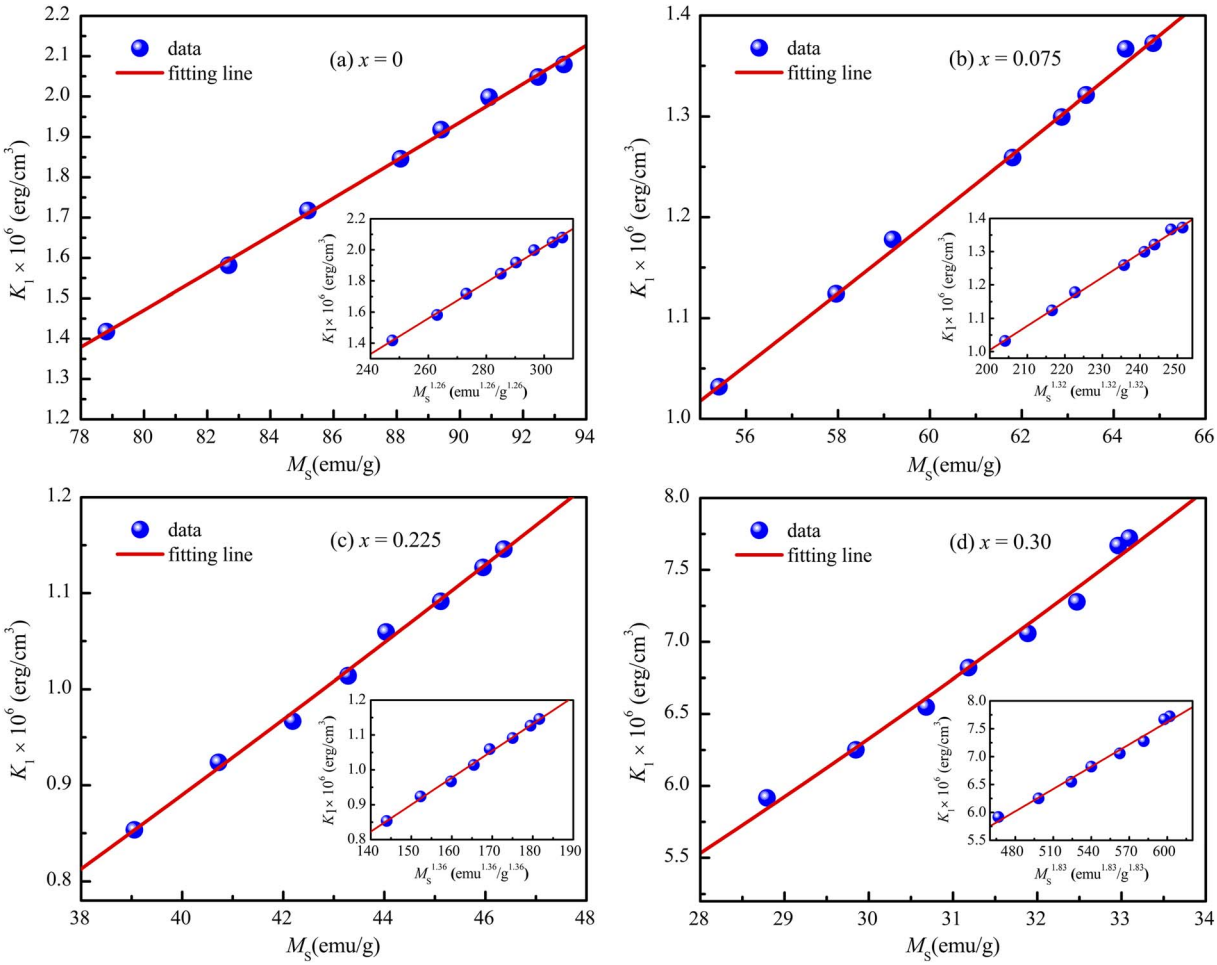

Fig. 9 Dependence of the magnetocrystalline anisotropy constant $K_1(T)$ on the saturation magnetization $M_s(T)$ for $Fe_{3-x}Lu_xO_4$ nanoparticles with (a) $x = 0$, (b) $x = 0.075$, (c) $x = 0.225$, and (d) $x = 0.30$. The main panel shows the scaling behavior $K_1 \propto M_s$ across all compositions, illustrating the compositional evolution of the scaling exponent q. The insets present linear fits of $K_1(T)$ *versus* $M_s^q(T)$ for each sample, from which the corresponding q values are extracted.

magnetocrystalline anisotropy, which cannot be described solely by the ion-originated anisotropic contribution assumed in the original model. Similar departures from the canonical $K_1 \propto M_s^q$ law have been reported in ferrimagnetic spinels, chemically substituted alloys, and composite systems where heavy nonmagnetic ions distort the local crystal field and modify the spin–orbit-driven anisotropy landscape.[47–51]

For nanocrystalline ferrites, however, the dominant mechanism responsible for the breakdown of the Callen–Callen law is the strong finite-size and surface anisotropy effects. The large surface-to-volume ratio enhances the contribution of surface anisotropy (K_s), whose temperature dependence differs fundamentally from that of bulk magnetocrystalline anisotropy. Theoretical studies have shown that K_s, suppresses the surface magnetization more rapidly with increasing temperature, thereby reducing the effective scaling exponent q well below the bulk limit.[52–54] This effect is further amplified by surface spin canting and structural relaxation at the particle boundary.

Consequently, the sub-theoretical q values observed in $Fe_{3-x}Lu_xO_4$ nanoparticles are primarily governed by the strong surface contribution to the effective anisotropy and by finite-size effects, consistent with trends observed in other nanosized ferrites such as $NiFe_2O_4$ [55] and $MnFe_2O_4$.[56] These findings indicate that the anisotropy behavior in Lu-doped ferrites cannot be captured by the simplified assumptions of the Callen–Callen model and instead reflects the complex interplay between bulk, surface, and exchange-mediated anisotropy contributions intrinsic to nanoscale spinel systems.

The temperature dependence of K_1 in ferrimagnetic spinels can be examined within the framework established for cubic ferromagnets. Brukhatov and Kirensky[57] originally proposed that $K_1(T)$ follows an empirical quadratic temperature dependence of the form:

$$K_1(T)/K_1(0) = \exp(-\alpha T^2) \quad (4)$$

Since the saturation magnetization $M_s(T)$ obeys Bloch's law for spin-wave excitations, Shenker[57] further showed that the corresponding temperature evolution of K_1 can be expressed as:

$$K_1(T)/K_1(0) = (1 - AT^{3/2})^q \sim \exp(-qAT^{3/2}), \quad (5)$$

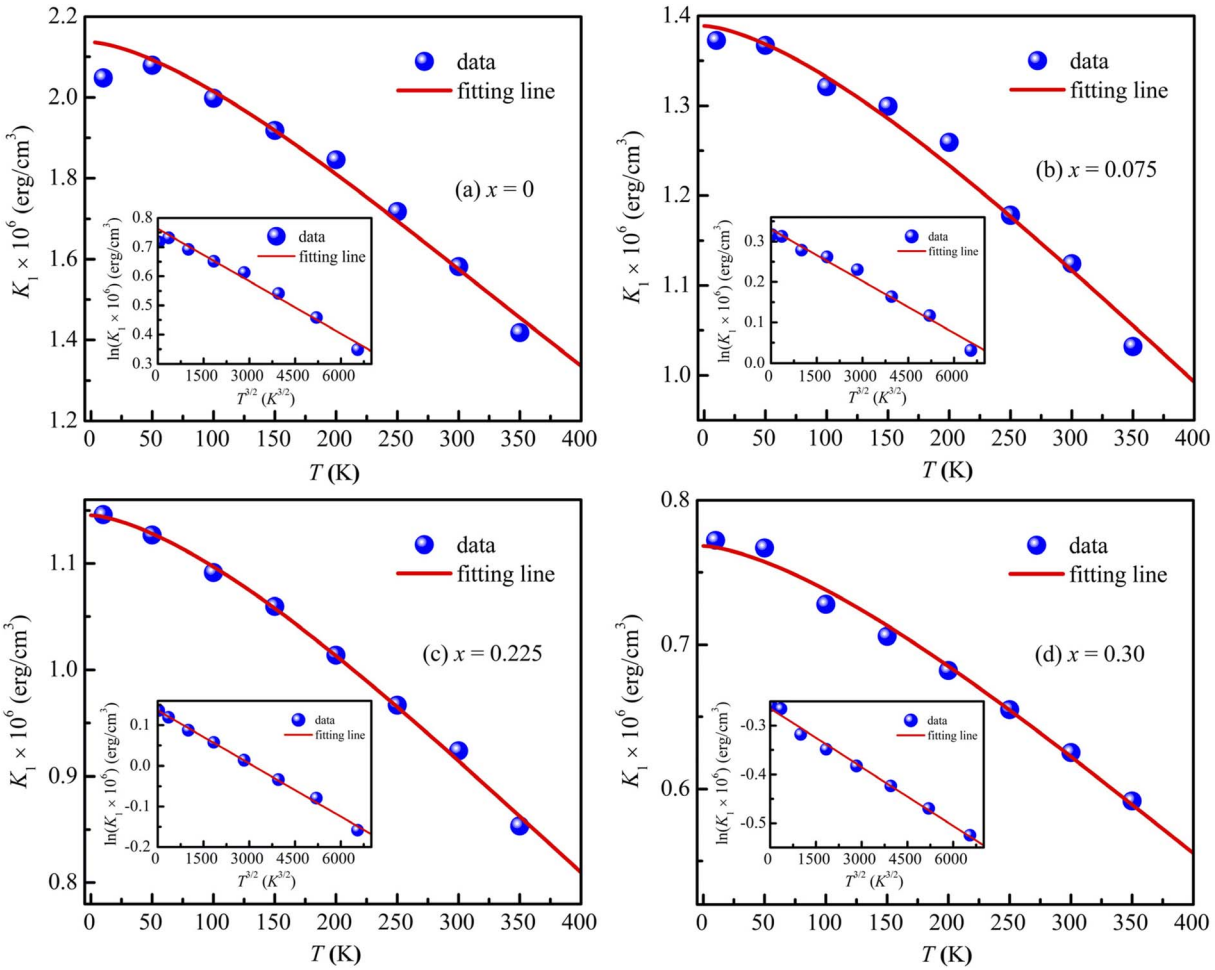

Fig. 10 Temperature dependence of the magnetocrystalline anisotropy constant $K_1(T)$ for the $Fe_{3-x}Lu_xO_4$ nanoparticles with (a) $x = 0$, (b) $x = 0.075$, (c) $x = 0.225$, and (d) $x = 0.30$. The solid curves represent fits to the eqn (4) in text, derived from the combined Bloch–Callen–Callen framework. The inset displays the linear dependence of $\ln(K_1)$ on $T^{3/2}$, demonstrating that the empirical temperature scaling of K_1 is well described by the Bloch-type spin-wave contribution to the magnetization.

where q is the scaling exponent associated with the ratio between magnetocrystalline anisotropy and magnetization.

Using this expression, the temperature dependence of K_1 for $Fe_{3-x}Lu_xO_4$ nanoparticles was analyzed, as shown in Fig. 10. The inset demonstrates a clear linear dependence of $\ln(K_1)$ on $T^{3/2}$, consistent with the expected Bloch-like behavior. These data are consistent with the correlation between K_1 and M_s established in the previous section. In classical studies on cobalt and nickel ferrites, Shenker observed that K_1 exhibits both a quadratic ($\propto T^2$) and a Bloch-type ($\propto T^{3/2}$) temperature dependence, although the experimental data at that time could not unambiguously distinguish the dominant mechanism. Subsequent investigations favored the quadratic form.[58,59] However, theories of ferromagnetic anisotropy have not been rigorously extended to ferrimagnetic spinels, particularly at the nanoscale where surface and finite-size effects become prominent.

The present results provide additional evidence that $K_1(T)$ in $Fe_{3-x}Lu_xO_4$ nanoparticles follows a Bloch-derived exponential dependence, consistent with a spin-wave-mediated reduction of anisotropy at low temperatures. This demonstrates that, despite structural complexity and multi-sublattice ferrimagnetism, the essential temperature dependence of magnetocrystalline anisotropy in these nanostructured ferrites aligns with models originally developed for conventional ferromagnetic materials.

IV. Conclusions

In this work, the microscopic origin of the magnetostructural evolution in $Fe_{3-x}Lu_xO_4$ nanoparticles has been systematically investigated using complementary X-ray and neutron diffraction, Mössbauer spectroscopy, and magnetic measurements. The results demonstrate that Lu^{3+} ions preferentially occupy the octahedral B sites, leading to lattice expansion and a concomitant weakening of the dominant A–B superexchange interaction (J_{AB}). This disruption of exchange pathways results in a progressive suppression of long-range ferrimagnetic ordering and the emergence of enhanced superparamagnetic behavior at room temperature.

Importantly, the observed reduction in saturation magnetization and the concurrent increase in coercivity cannot be attributed solely to magnetic dilution. Instead, they arise from

a coupled interplay between exchange weakening, local structural distortions, and surface-induced spin disorder, which collectively govern the magnetic energy landscape at the nanoscale. The significant deviation of the effective anisotropy constant $K_1(T)$ from the Callen–Callen power-law behavior (q = 1.26–1.83) further confirms the breakdown of ideal spin-coherent rotation and indicates the dominant role of finite-size effects and non-collinear surface spin configurations.

Overall, these findings provide a unified picture in which the magnetic response of Lu-doped Fe_3O_4 nanoparticles is not governed by a single substitutional effect, but by the cooperative competition between exchange interactions, structural perturbations, and surface spin disorder. This perspective reconciles key aspects of previously reported inconsistencies in RE-doped ferrite systems and highlights the limitations of simplified site-occupancy-based interpretations in describing nanoscale magnetism.

Author contributions

N. T. Dang: writing – original draft, investigation, formal analysis; D. P. Kozlenko, S. E. Kichanov, N. H. Nam and A. L. Zhaludkevich: writing – review and editing, methodology, conceptualization; N. D. Minh, N. T. Nguyen, T. A. Tran, Y. D. Mitskevich, A. A. Kharchanka and J. A. Fedotova: investigation, formal analysis; writing – review and editing; Pham Thanh Phong: writing – original draft, writing – review and editing, methodology, conceptualization; A. V. Rutkauskas, D. P. T. Tien, G. S. Rymski and Truong-Tho Nguyen: writing – original draft, writing – review and editing, methodology, conceptualization, supervision, funding acquisition.

Conflicts of interest

The authors declare that they have no known competing financial interests or personal relationships that could have appeared to influence the work reported in this paper.

Data availability

The data that support the findings of this study are available from the authors upon reasonable request.

Supplementary information (SI) is available. See DOI: https://doi.org/10.1039/d6ra05041g.

Acknowledgements

The investigation of the magnetic properties was supported by the financial support of the Vietnam Academy of Science and Technology (grant No. VAST 03.07/25-26) and the Vietnam Ministry of Education and Training under the grant No. B2026-DHH-03. The X-ray and neutron diffraction experiments have been supported by the joint grants the Russian Science Foundation, RSF 24-42-10003, https://rscf.ru/project/24-42-10003/ and the Belarusian Foundation for Basic Research, BFBR T23RNFM-023. N. T. Nguyen was funded by the PhD Scholarship Programme of Vingroup Innovation Foundation (VINIF), VinUniversity, code VINIF.2025.TS26.

References

1 G. Singh, H. Chan, A. Baskin, E. Gelman, N. Repnin, P. Král and R. Klajn, *Science*, 2014, **345**, 1149–1153.
2 I. C. Lekshmi, R. Buonsanti, C. Nobile, R. Rinaldi, P. D. Cozzoli and G. Maruccio, *ACS Nano*, 2011, **5**, 1731–1738.
3 S. Ohkoshi, A. Namai, M. Yoshikiyo, K. Imoto, K. Tamazaki, K. Matsuno, O. Inoue, T. Ide, K. Masada, M. Goto, T. Goto, T. Yoshida and T. Miyazaki, *Angew. Chem.*, 2016, **128**, 11575–11578.
4 S. Jonak and J. P. Borah, *Mater. Today Commun.*, 2021, **26**, 101789.
5 Y. Huang, L. Li, D. Zhang, L. Gan, P. Zhao, Y. Zhang, Q. Zhang, M. Hua and C. Jia, *Magn. Reson. Imaging*, 2020, **68**, 113–120.
6 Y. Yang, M. Huang, J. Qian, D. Gao and X. Liang, *Sci. Rep.*, 2020, **10**, 8331.
7 H. Peng, G. Ren, N. Hampp, A. Wu and F. Yang, *Nanoscale*, 2023, **15**, 10513–10528.
8 S. S. Laha, N. D. Thorat, G. Singh, C. I. Sathish, J. Yi, A. Dixit and A. Vinu, *Small*, 2022, **18**, 2104855.
9 J. Sanchez-Marcos, E. Mazario, J. A. Rodriguez-Velamazan, E. Salas, P. Herrasti and N. Menendez, *J. Alloys Compd.*, 2018, **739**, 909–917.
10 Y. V. Kolen'Ko, M. Bañobre-López, C. Rodríguez-Abreu, E. Carbó-Argibay, A. Sailsman, Y. Piñeiro-Redondo, M. F. Cerqueira, D. Y. Petrovykh, K. Kovnir, O. I. Lebedev and J. Rivas, *J. Phys. Chem. C*, 2014, **118**, 8691–8701.
11 L. Tan, A. V. Sapelkin, A. J. Misquitta, C. L. Bull, H. Lin, H. Tian, H. Huang and M. T. Dove, *Appl. Phys. Lett.*, 2022, **120**, 233101.
12 T. Kmječ, N. T. Nghiem, N. Truong-Tho, D. P. Kozlenko, S. E. Kichanov, A. V. Rutkauskas, V. T. Nguyen, E. A. Korneeva, D. T. Khan, D. T. Huong Giang, T. L. Phan, D. D. Bich, G. S. Rymski, J. Kohout, V. Chlan and N. T. Dang, *Ceram. Int.*, 2025, **51**, 5168–5180.
13 O. Dehghani Dastjerdi, H. Shokrollahi and S. Mirshekari, *Inorg. Chem. Commun.*, 2023, **153**, 110797.
14 P. Kowalik, J. Mikulski, A. Borodziuk, M. Duda, I. Kamińska, K. Zajdel, J. Rybusinski, J. Szczytko, T. Wojciechowski, K. Sobczak, R. Minikayev, M. Kulpa-Greszta, R. Pazik, P. Grzaczkowska, K. Fronc, M. Lapinski, M. Frontczak-Baniewicz and B. Sikora, *J. Phys. Chem. C*, 2020, **124**, 6871–6883.
15 K. P. Hazarika and J. P. Borah, *J. Magn. Magn. Mater.*, 2022, **560**, 169597.
16 A. Rękorajska, G. Cichowicz, M. K. Cyranski, M. Pękała and P. Krysinski, *J. Magn. Magn. Mater.*, 2019, **479**, 50–58.
17 H. Xiang, P. Dong, Z. Wang, T. Zhang, C. Lu, G. Jin and Y. Wang, *J. Alloys Compd.*, 2020, **847**, 156549.
18 J. C. Park, J. K. Park, G. T. Lee, D. H. Kim, H. Cha, T. Y. Park, M. Kim, Y. Chang, H. J. Cha and J. H. Seo, *J. Ind. Eng. Chem.*, 2019, **77**, 408–415.

19 D. Kozlenko, S. Kichanov, E. Lukin and B. Savenko, *Crystals*, 2018, **8**, 331.
20 J. Rodríguez-Carvajal, *Phys. B*, 1993, **192**, 55–69.
21 K. Lagarec and D. G. Rancourt, *Recoil-Mössbauer Spectral Analysis Software for Windows*, University of Ottawa, Ottawa, 1998.
22 T. H. Ting, *Results Phys.*, 2020, **16**, 102975.
23 C. A. Schneider, W. S. Rasband and K. W. Eliceiri, *Nat. Methods*, 2012, **9**, 671–675.
24 S. Klotz, G. Steinle-Neumann, T. Strässle, J. Philippe, T. Hansen and M. J. Wenzel, *Phys. Rev. B: Condens. Matter Mater. Phys.*, 2008, **77**, 012411.
25 V. Biju, N. Sugathan, V. Vrinda and S. L. Salini, *J. Mater. Sci.*, 2008, **43**, 1175–1179.
26 E. J. Mittemeijer and U. Welzel, *Z. Kristallogr.*, 2008, **223**, 552–560.
27 H. L. Andersen, C. Granados-Miralles, K. M. Ø. Jensen, M. Saura-Múzquiz and M. Christensen, *ACS Nano*, 2024, **18**, 9852–9870.
28 B. L. Cushing, V. L. Kolesnichenko and C. J. O'Connor, *Chem. Rev.*, 2004, **104**, 3893–3946.
29 D. P. Kozlenko, L. S. Dubrovinsky, S. E. Kichanov, E. V. Lukin, V. Cerantola, A. I. Chumakov and B. N. Savenko, *Sci. Rep.*, 2019, **9**, 4464.
30 J. Mohapatra, M. Xing, J. Beatty, J. Elkins, T. Seda, S. R. Mishra and J. P. Liu, *Nanotechnology*, 2020, **31**, 275706.
31 I. Castellanos-Rubio, O. Arriortua, D. Iglesias-Rojas, A. Barón, I. Rodrigo, L. Marcano, J. S. Garitaonandia, I. Orue, M. L. Fdez-Gubieda and M. Insausti, *Chem. Mater.*, 2021, **33**, 8693–8704.
32 W. Geertsma and D. Khomskii, *Phys. Rev. B: Condens. Matter Mater. Phys.*, 1996, **54**, 3011–3014.
33 T. D. Thanh, T. T. Ngoc Nha, T. T. Ha Giang, P. H. Nam, D. N. Toan, D. T. Khan, D. H. Manh and P. T. Phong, *RSC Adv.*, 2024, **14**, 23645–23660.
34 S. T. Xu, Y. Q. Ma, G. H. Zheng and Z. X. Dai, *Nanoscale*, 2015, **7**, 6520–6526.
35 E. F. Kneller and F. E. Luborsky, *J. Appl. Phys.*, 1963, **34**, 656–658.
36 S. Yoon, *J. Korean Phys. Soc.*, 2011, **59**, 3069–3073.
37 R. Grössinger, *Phys. Status Solidi A*, 1981, **66**, 665–674.
38 K. M. Krishnan, *Fundamentals and Applications of Magnetic Materials*, Oxford University Press, 2016.
39 C. Kittel, *Introduction to Solid State Physics*, Wiley, 2018.
40 A. Franco, F. L. A. MacHado and V. S. Zapf, *J. Appl. Phys.*, 2011, **110**, 053913.
41 Y. Yafet and C. Kittel, *Phys. Rev.*, 1952, **87**, 290–294.
42 E. C. Stoner and E. P. Wohlfarth, *Philos. Trans. R. Soc. London, Ser. A*, 1948, **240**, 599–642.
43 I. Panneer Muthuselvam and R. N. Bhowmik, *J. Magn. Magn. Mater.*, 2010, **322**, 767–776.
44 T. Hyeon, Y. Chung, J. Park, S. S. Lee, Y.-W. Kim and B. H. Park, *J. Phys. Chem. B*, 2002, **106**, 6831–6833.
45 S. Laureti, G. Varvaro, A. M. Testa, D. Fiorani, E. Agostinelli, G. Piccaluga, A. Musinu, A. Ardu and D. Peddis, *Nanotechnology*, 2010, **21**, 315701.
46 H. B. Callen and E. Callen, *J. Phys. Chem. Solids*, 1966, **27**, 1271–1285.
47 Á. Buruzs, P. Weinberger, L. Szunyogh, L. Udvardi, P. I. Chleboun, A. M. Fischer and J. B. Staunton, *Phys. Rev. B: Condens. Matter Mater. Phys.*, 2007, **76**, 064417.
48 J. B. Staunton, L. Szunyogh, A. Buruzs, B. L. Gyorffy, S. Ostanin and L. Udvardi, *Phys. Rev. B: Condens. Matter Mater. Phys.*, 2006, **74**, 144411.
49 O. N. Mryasov, U. Nowak, K. Y. Guslienko and R. W. Chantrell, *Europhys. Lett.*, 2005, **69**, 805–811.
50 N. H. Hai, N. M. Dempsey and D. Givord, *IEEE Trans. Magn.*, 2003, **39**, 2914–2916.
51 R. Skomski, A. Kashyap and J. Zhou, *Scr. Mater.*, 2005, **53**, 389–394.
52 R. Yanes, O. Chubykalo-Fesenko, R. F. L. Evans and R. W. Chantrell, *J. Phys. D: Appl. Phys.*, 2010, **43**, 474009.
53 D. A. Garanin and H. Kachkachi, *Phys. Rev. Lett.*, 2003, **90**, 065504.
54 H. Kachkachi and E. Bonet, *Phys. Rev. B: Condens. Matter Mater. Phys.*, 2006, **73**, 224402.
55 B. K. Chatterjee, C. K. Ghosh and K. K. Chattopadhyay, *J. Appl. Phys.*, 2014, **116**, 153904.
56 T. T. N. Nha, D. N. Toan, D. T. Khan, L. T. T. Ngan, L. V. Bau, T. D. Thanh, D. H. Manh, P. T. Phong and N. X. Phuc, *Ceram. Int.*, 2025, **51**, 50091–50102.
57 H. Shenker, *Phys. Rev.*, 1957, **107**, 1246–1249.
58 S. Menchaca-Nal, J. A. Jativa-Herrera, O. Moscoso-Londoño, L. G. Pampillo, R. Martínez-García, M. Knobel and C. L. Londoño-Calderón, *Mater. Chem. Phys.*, 2023, **303**, 127798.
59 J. A. Ramos-Guivar, A. C. Krohling, E. O. López, F. Jochen Litterst and E. C. Passamani, *J. Magn. Magn. Mater.*, 2019, **485**, 142–150.